ICON: The Icosahedral Nonhydrostatic Modelling Framework of DWD and MPI-M

Günther Zängl

Deutscher Wetterdienst, Frankfurter Str. 135
63067 Offenbach, Germany
Guenther.Zaengl@dwd.de

ABSTRACT

This article gives an overview of the Icosahedral Nonhydrostatic (ICON) Modelling Framework, which is being developed in a collaboration between the German Weather Service (DWD) and Max-Planck Institute for Meteorology (MPI-M) in order to establish a unified modelling system for numerical weather prediction and climate modelling. After a brief description of the dynamical core, the grid-nesting approach and the physics parametrization package, a selection of idealized validation tests as well as NWP scores comparing ICON with the currently operational hydrostatic global model GME are presented. The results reveal that ICON achieves better skill scores at reduced computational cost. Moreover, it is shown that the dynamical core of ICON is well prepared for future use at truly nonhydrostatic scales, being able to cope with much steeper mountains than is typical for models with terrain-following coordinates.

1 Introduction

In 2001, the Max-Planck Institute for Meteorology (MPI-M) and the German Weather Service (DWD) agreed upon a collaboration to develop a unified modelling framework for numerical weather prediction (NWP) and climate applications. The planning started with compiling a list of mandatory and/or desirable properties of the common modelling system, the most important of which are summarized here:

- Development of a nonhydrostatic dynamical core in order to allow using the model over the full range of spatial resolutions relevant for NWP.
- Exact numerical conservation of atmospheric variables that are conserved in nature: this goal was formulated as mandatory for mass and as desirable for energy. In addition, mass-consistent transport of tracer variables was requested, which is particularly crucial for chemistry modelling because chemical reactions can depend very sensitively on the relative mixing ratios of the participating constituents, but also important for NWP because spurious sources or sinks in the moisture budget potentially deteriorate the forecast quality.
- Conservative atmosphere-ocean coupling: achieving this goal without highly sophisticated remapping algorithms requires computing the atmosphere and ocean components of the modelling system on conforming grids. Therefore, an ocean circulation model using (basically) the same grid structure as the atmospheric component presented here is being developed as well.
- The availability of some means of static mesh refinement, which was subsequently concretized into the capability of mixing one-way nested and two-way nested grids within one model application, combined with an option for vertical nesting in order to allow nested domains having a lower

top than the global domain. In addition, a limited-area mode was considered as highly desirable in order to allow establishing a completely unified modelling system in the longer-term future.

- High efficiency and scalability on future massively parallel high-performance computing architectures with O(10^4+) cores; in particular, elliptic solvers involving either global communication or frequent halo communication were regarded as disadvantageous.

At DWD, it is currently planned to replace the operational hydrostatic global model GME (Majewski et al., 2002), running at a mesh size of 20 km with 60 vertical levels up to 5 hPa, with a non-nested configuration of ICON (13 km mesh size, 90 levels up to 75 km) by the end of 2014. About half a year later, it is planned to activate a nested domain over Europe with a mesh size of 6.5 km in order to replace the regional model COSMO-EU (7 km, 40 levels up to 23 km) as well. Besides an expected improvement of the forecast quality, this will reduce the complexity of the operational NWP suite at DWD. Likewise, at MPI-M, the coupled atmosphere-ocean climate modelling system ECHAM-MPIOM will be replaced by a coupled model within the ICON framework. In addition, the regional climate model REMO, which builds upon the old hydrostatic regional weather forecasting model EM/DM of DWD, is planned to be replaced by ICON using the limited-area mode.

The remainder of this paper is structured as follows. Section 2 will provide a brief description of the dynamical core, the grid-nesting strategy and the physics package envisaged for NWP. Selected results from a hierarchy of tests, ranging from idealized dynamical core tests to NWP applications will be presented in section 3. The paper closes with a set of conclusions in section 4.

2 Model description

2.1 Grid generation

The discretization of the model equations of ICON is performed on an icosahedral-triangular Arakawa-C grid. The mass points are located in the circumcenter of each triangular cell, and the edge-normal horizontal velocity component is defined at the edge midpoints. The grid generation is based on the successive refinement of a spherical icosahedron. In the so-called root division step, the edges of each basic triangle are divided into n equal arcs. Connecting the new edge points by great circle arcs yields n^2 spherical triangles within the original triangle. This step is followed by k bisection steps, where each triangle is consecutively subdivided into 4 smaller triangles. The resulting total number of cells n_c and edges n_e is then given by

$$n_c = 20n^2 4^k; \qquad n_e = 30n^2 4^k, \tag{1}$$

and the corresponding effective mesh size of the model grid is computed as $\sqrt{4\pi r_e^2/n_c}$, where r_e denotes the radius of the earth. A more detailed description of the model grid including graphical illustrations is provided by Wan et al. (2013).

2.2 Dynamical core

The ICON model solves the fully compressible nonhydrostatic atmospheric equations of motion, using the set of prognostic variables suggested by Gassmann and Herzog (2008), but a two-dimensional rather than a three-dimensional Lamb transformation to convert the nonlinear momentum advection into a vector-invariant form. The basic equation system reads as follows

$$\frac{\partial v_n}{\partial t} + \frac{\partial K_h}{\partial n} + (\zeta + f)v_t + w\frac{\partial v_n}{\partial z} = -c_{pd}\theta_v \frac{\partial \pi}{\partial n} + F(v_n) \tag{2}$$

$$\frac{\partial w}{\partial t} + \mathbf{v_h} \cdot \nabla w + w \frac{\partial w}{\partial z} = -c_{pd} \theta_v \frac{\partial \pi}{\partial z} - g \tag{3}$$

$$\frac{\partial \rho}{\partial t} + \nabla \cdot (\mathbf{v} \rho) = 0 \tag{4}$$

$$\frac{\partial \rho \theta_v}{\partial t} + \nabla \cdot (\mathbf{v} \rho \theta_v) = \tilde{Q} \tag{5}$$

To simplify the implicit numerical treatment of the terms representing vertical sound wave propagation, equation (5) is rewritten as

$$\frac{\partial \pi}{\partial t} + \frac{R_d}{c_{vd}} \frac{\pi}{\rho \theta_v} \nabla \cdot (\mathbf{v} \rho \theta_v) = \hat{Q} \tag{6}$$

The prognostic variables of the equation system are the horizontal velocity component normal to the triangle edges v_n, the vertical wind component w, density ρ, and virtual potential temperature θ_v. The reconstructed tangential velocity component is denoted as v_t, and to be consistent with the model code, it is assumed that (v_t, v_n, w) form a right-handed system. $\mathbf{v_h}$ and $\mathbf{v}$ denote the horizontal and three-dimensional wind vector, respectively. The remaining symbols are the vertical vorticity component ζ, the Coriolis parameter f, the horizontal part of the kinetic energy $K_h = \frac{1}{2}(v_n^2 + v_t^2)$, the Exner function π, the specific heat capacities of dry air at constant pressure c_{pd} and volume c_{vd}, the gas constant of dry air $R_d = c_{pd} - c_{vd}$, and the gravitational acceleration g. $\frac{\partial}{\partial n}$ denotes a horizontal derivative in edge-normal direction, i.e. between the two adjacent mass points. Moreover, $F(v_n)$ denotes source terms for horizontal momentum (e.g. from physics parametrizations), and $\tilde{Q}$ and $\hat{Q}$ denote appropriately formulated diabatic heat source terms.

A description and illustration of the basic horizontal operators is given in Wan et al. (2013). Note that the flux form of equations (4) and (5) provides a straightforward way to achieve local mass conservation to machine precision. Time integration is accomplished with a two-time-level predictor-corrector scheme that is explicit except for the terms describing vertical sound-wave propagation. The decision for this scheme is motivated by the fact that for a global model that is supposed to extend up to the mesosphere, a split-explicit scheme does not pay off because the ratio between sound speed and the maximum wind speed is not large enough. Instead, we apply a time splitting between the dynamical core and the physics parametrizations including tracer advection. The time-step ratio is typically 4 or 5.

To allow for mass-consistent tracer transport, the air mass fluxes are aggregated over the small time steps in the dynamical core and then passed to the transport scheme. Tracer transport is performed with a flux-form semi-Lagrangian scheme following Miura (2007) with options for second-order and third-order accuracy for horizontal transport. The second-order variant is also used in the dynamical core for ρ and θ_v. For vertical transport, a piecewise parabolic reconstruction of the sub-grid tracer distribution provides third-order accuracy, and an option for summation of partial fluxes allows vertical CFL numbers much larger than 1. For horizontal and vertical transport, monotonous and positive definite limiters are available. Further information on the horizontal transport scheme, and a set of idealized validation tests, can be found in Lauritzen et al. (2013).

2.3 Grid nesting

The grid-nesting approach adopted in ICON is a classical two-way nesting. To (largely) circumvent the problem of unphysical wave reflections at the nest boundaries, the mesh-size ratio is fixed to a value of 2, which means that one large triangular cell (denoted as parent cell in the following) is subdivided by edge bisection into four small triangular (child) cells. To ensure numerical stability with explicit time-stepping, the time step in nested domain(s) is reduced in proportion to the mesh refinement ratio. The nesting works recursively for multiple nesting levels, and multiple nested domains per nesting level (i.e. having the same mesh size) as well as geometrically non-contiguous nested domains are also allowed. In addition, vertical nesting is available, which means that a nested domain may have a lower top level

than the parent domain. The flow control of the nesting is implemented in a way that the ICON model can also be used in a limited-area mode, in which the parent-to-child boundary interpolation (see below) is replaced by specifying the lateral boundary conditions from external data. The coupling step between successive nesting levels is the large (physics) time step of the respective parent domain. The basic workflow at model runtime is thus as follows:

- Integrate one physics time step in the parent domain.
- Compute the lateral boundary conditions for the nested domain(s).
- Integrate two physics time steps in the nested domain(s).
- Provide feedback from the nested domain(s) to the parent domain

The interpolation of the prognostic variables to the lateral boundaries of the nested domain is based primarily on the use of RBFs (radial basis functions). For mass point variables, the procedure starts with reconstructing the two-dimensional horizontal gradient at the mass point of the parent cell, which is then used to extrapolate the variable from the parent cell mass point to each child cell lying within a parent cell. For velocities and mass fluxes, a distinction is made between child edges lying on a parent edge and those lying in the interior of a parent cell. On the latter, a direct RBF interpolation is applied, whereas the calculation for the former points starts with a vector reconstruction of the variable at the vertices of each cell, followed by an extrapolation from the parent edge to the child edges using the tangential gradient of the variable. This way, it is ensured that the mass flux across a nest interface edge on the parent grid is exactly the same as the sum of the fluxes across the corresponding edges of the child grid.

The feedback of the prognostic variables is implemented as a Rayleigh relaxation of the parent-grid variables to an appropriate average of the child-grid variables. A direct incremental feedback is also available but not used in real-case applications because it suffers from numerical stability problems when combined with vertical nesting. When the one-way nesting option is chosen, the feedback is turned off. Instead, a nudging of the child-grid variables towards the parent-grid variables is applied in this case near the lateral nest boundaries in order to prevent inconsistencies.

2.4 Physics-dynamics coupling

The physics-dynamics coupling in ICON differs from most other models in that it is performed at constant density (volume) rather than constant pressure. This is related to the fact that the total air density ρ is one of the prognostic variables, whereas pressure is only diagnosed for parametrizations needing pressure as an input variable. As a consequence, heating rates arising from radiative flux divergences or latent heat release have to be converted into temperature changes using c_v, the specific heat capacity at constant volume of moist air. Some physics parametrizations inherited from hydrostatic models, in which the physics-dynamics coupling always assumes constant pressure, therefore had to be adapted appropriately. To optimize runtime efficiency, there is a distinction between so-called fast-physics processes (e.g. cloud microphysics, turbulence), which are calculated at every physics time step, and slow-physics processes (e.g. radiation), which may be called at longer time steps and provide tendencies to the dynamical core that remain constant between two successive calls of the parametrization. Fast-physics processes are treated with operator splitting, which means that they act on an atmospheric state that has already been updated by the dynamical core, horizontal diffusion and the tracer transport scheme. Each process then sequentially updates the atmospheric variables and passes a new state to the subsequent parametrization.

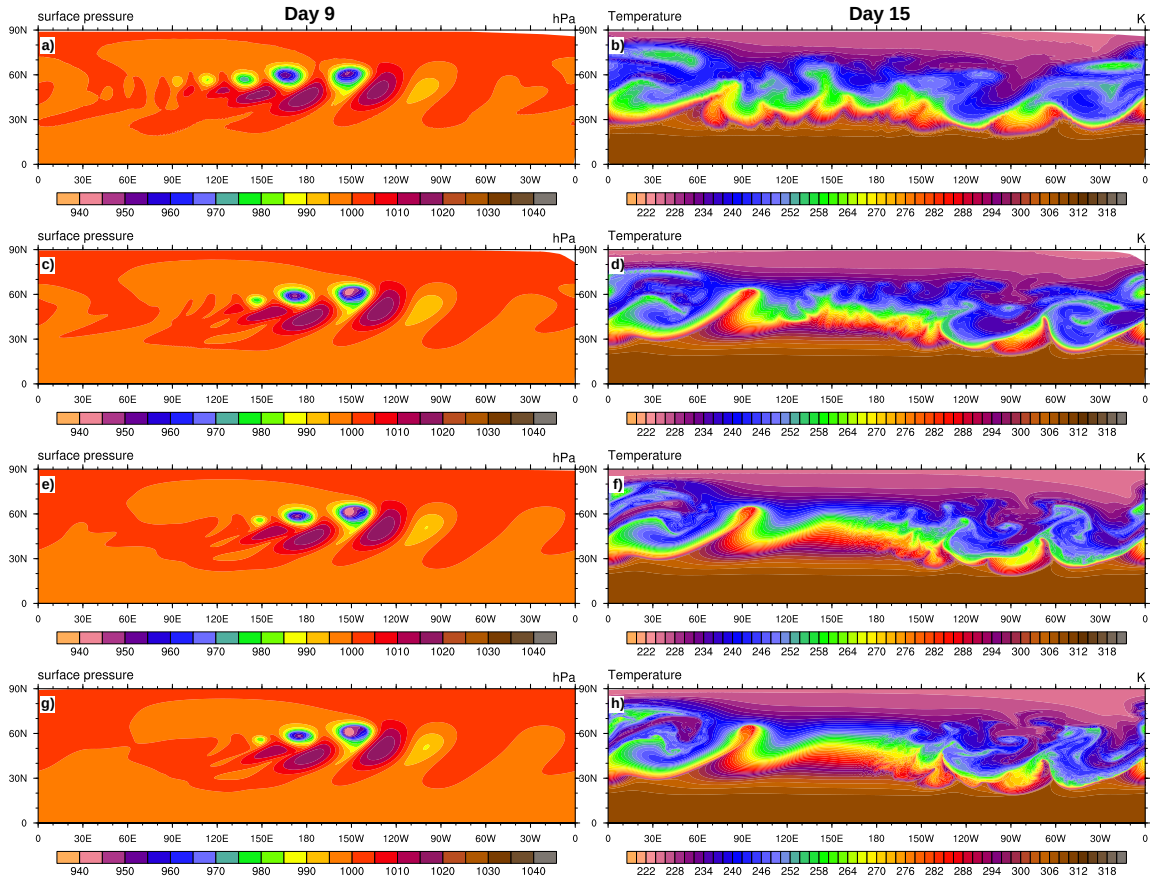

Figure 1: Surface pressure after 9 days of simulation (left panels), and temperature at about 1550 m AGL after 15 days of simulation (right panels) for model resolutions of (a,b) 160 km*, (c,d)* 80 km*, (e,f)* 40 km *and (g,h)* 20 km*.*

2.5 Physics parametrizations

The physics parametrizations used in ICON have been partly imported from the COSMO model and partly from the IFS, with the exception of the saturation adjustment that had to be rewritten for ICON due to the above-mentioned constant-volume coupling. From the COSMO model, we inherited the five-category cloud microphysics scheme that is operational in the COSMO-EU (Doms and Schättler, 2004; Seifert, 2008), the TKE-based turbulence scheme (Raschendorfer, 2001) and the TERRA land-surface scheme (Heise et al., 2006). From the IFS, we imported the moist convection scheme (Bechtold et al., 2008), the subgrid-scale orography scheme (Lott and Miller, 1997) and the nonorographic gravity-wave drag scheme (Orr et al., 2010). Moreover, the RRTM radiation scheme (Mlawer et al., 1997) is used in a similar version as in the IFS.

3 A hierarchy of tests

3.1 Jablonowski-Williamson test

The Jablonowski and Williamson (2006) baroclinic wave test is nowadays considered as a standard test for dynamical cores in global models. The basic state is a zonally symmetric, strongly baroclinic atmosphere with a surface equator-to-pole temperature contrast of about 80 K. It is in hydrostatic and

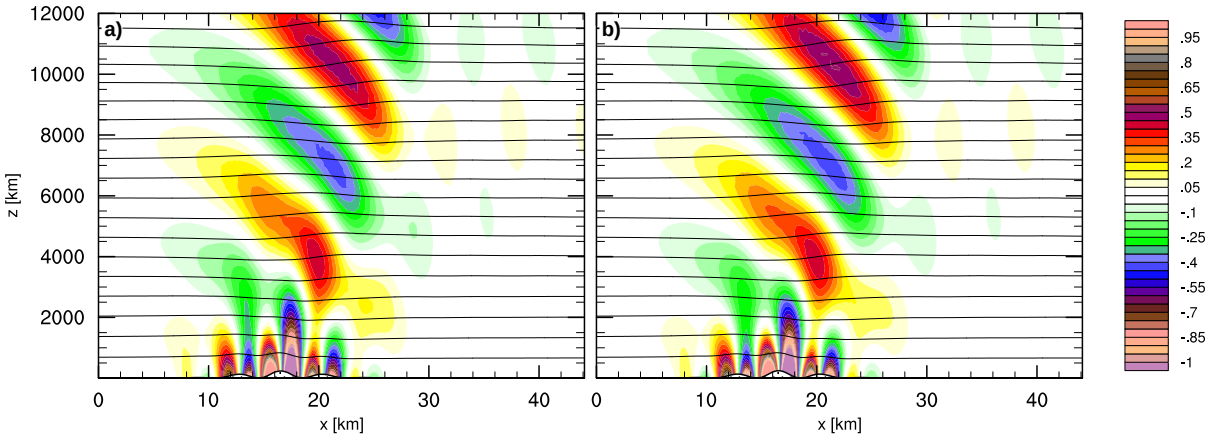

Figure 2: Vertical velocity for the Schär et al. (2002) mountain-wave test after 12 hours of integration, using mesh sizes of (a) $\Delta x = 625\,\mathrm{m}$ *and (b)* $\Delta x = 312\,\mathrm{m}$*. The contour interval is* $0.05\,\mathrm{m/s}$*.*

geostrophic balance at initial time, but a weak perturbation is imposed on the wind field at 20°N, 40°E that triggers a sequence of intense baroclinic waves during the course of the simulation. At coarse mesh sizes resolving the baroclinic waves only marginally, this test highlights the diffusivity (or effective resolution) of a dynamical core, and the presence of phase speed errors in the advection of poorly resolved structures. Moreover, the evolution of the flow in the initially unperturbed southern hemisphere, or in the unperturbed steady-state variant of the test, reveals the presence of grid imprinting on the solution.

Fig. 1 displays the surface pressure on day 9 and the temperature at about 1550 m AGL on day 15. For the former quantity, reference results are available in Jablonowski and Williamson (2006) and several other publications. In agreement with the results from other models, it can be seen that the core pressure of the two main cyclones is not as low for 160 km (Fig. 1(a)) as for the higher resolutions (Fig. 1(c,e,g)). On the other hand, additional cyclonic disturbances are seen at the trailing edge of the wave train. The latter is related to grid imprinting, providing an additional triggering mechanism for cyclogenesis. Moreover, a phase error can be noticed for the 160-km run, with the middle and left cyclones being located farther west than for the higher resolutions. This corresponds to a too slow propagation speed and is a typical feature for models with finite-difference discretizations, whereas finite-volume and spectral transform models do not tend to suffer from substantial phase errors. The results for 40 km and 20 km (Fig. 1(e,g)) differ only in very minor details, indicating that they are almost converged. Much larger variability between the four model resolutions is seen for the temperature fields on day 15 (Fig. 1(b,d,f,h)), which is mainly a consequence of the longer period of nonlinear flow evolution. Nevertheless, most flow features look similar to each other for the two highest resolutions. In addition, there is a general tendency for the formation of sharper gradients and small-scale flow instabilities with increasing resolution.

3.2 Flow over small-scale mountains

Schär-mountain test

To verify that the metric terms related to the terrain-following coordinate transformation are discretized in a consistent manner, the so-called Schär-mountain test case (Schär et al., 2002) has been conducted. The test considers uniform flow with constant wind speed U and Brunt-Väisälä-frequency N over a

sequence of mountains defined by

$$h(x) = h_m \exp\left(-\frac{x^2}{a^2}\right) \cos^2 \frac{\pi x}{\lambda}\,. \tag{7}$$

With the usual parameter settings, h_m = 250 m, a = 5000 m, λ = 4000 m, $N = 10^{-2}\,\mathrm{s}^{-1}$ and $U = 10\,\mathrm{m\,s}^{-1}$, the mountain triggers a combination of small-scale, rapidly decaying nonhydrostatic gravity waves and a larger-scale, quasi-hydrostatic vertically propagating gravity wave. The latter tends to exhibit perturbations reflecting the structure of the small-scale mountains if the model equations are not discretized consistently. Results after 12 hours of integration are shown in Fig. 2 for mesh sizes of 625 m and 312 m, respectively. They can be compared against the linear analytical solution (Schär et al., 2002) and results from other numerical models, usually published for a mesh size of 500 m (Schär et al., 2002; Klemp and Skamarock, 2003; Skamarock et al., 2012). It is evident that no suspicious structures are generated over the mountain even at the coarser resolution. Both results compare favourably with the analytical solution, and there are only slight differences in the wave amplitude between $\Delta x = 625\,\mathrm{m}$ (Fig. 2a) and $\Delta x = 312\,\mathrm{m}$ (Fig. 2b), indicating that resolving the peak-to-peak distance λ of 4000 m with about six grid points is already sufficient for a reasonably accurate representation of the flow structure.

Pushing the limits of terrain-following coordinates

The ICON dynamical core has an option for a truly horizontal discretization of the horizontal pressure gradient term (Zängl, 2012), which allows it to handle very steep orography without suffering from numerical instabilities. This is demonstrated in Fig. 3, showing experiments for a circular Gaussian mountain

$$h(x,y) = h_m \exp\left(-\frac{x^2+y^2}{a^2}\right) \tag{8}$$

with $a = 2000\,\mathrm{m}$ and $h_m = 7000\,\mathrm{m}$. This corresponds to a maximum slope of 3, or a slope angle of 71°, which is way beyond what is commonly believed to be feasible with terrain-following coordinates. The results for an isothermal atmosphere at rest (Fig. 3a,b) show that even for this extraordinarily steep mountain, the spurious disturbances developing above the slopes are reasonably small. Thus, it can be expected that for more realistic configurations with non-zero ambient wind speed, the flow field over the mountain is not severely contaminated by numerical errors. In fact, the results for $U = 25\,\mathrm{m\,s}^{-1}$ (Fig. 3c,d) show only weak signals of suspicious structures. Apart from that, the vertical wind field (Fig. 3c) indicates a nonhydrostatic gravity wave propagating upward and downstream, which is in accordance with gravity-wave theory. In the lee of the mountain, flow reversal related to a pair of vortices forming on the cross-stream sides of the mountain induces strongly turbulent flow, which is also typical for strongly nonlinear flow around a mountain.

3.3 Towards operational NWP

To optimize the forecast quality of the ICON model and to support coupling ICON with DWD's 3D-Var data assimilation system currently used for the operational GME, regular test suites are conducted with interpolated IFS analysis data for January and June 2012. The ICON configuration used for the majority of the tests has a horizontal mesh size of 40 km (in order to save computing time) and 90 model levels with a top at 75 km. For direct comparability, a corresponding reference run has been conducted with the GME, also using a mesh size of 40 km and the operational 60-level setup with a top at 5 hPa.

A few selected results summarizing the status of September 2013 are displayed in Fig. 4. Verification is done every 12 forecast hours against IFS analysis data on a 1.5° latitude-longitude grid, following the respective WMO standard. For the 500-hPa geopotential scores shown in the figure, it can be seen that the

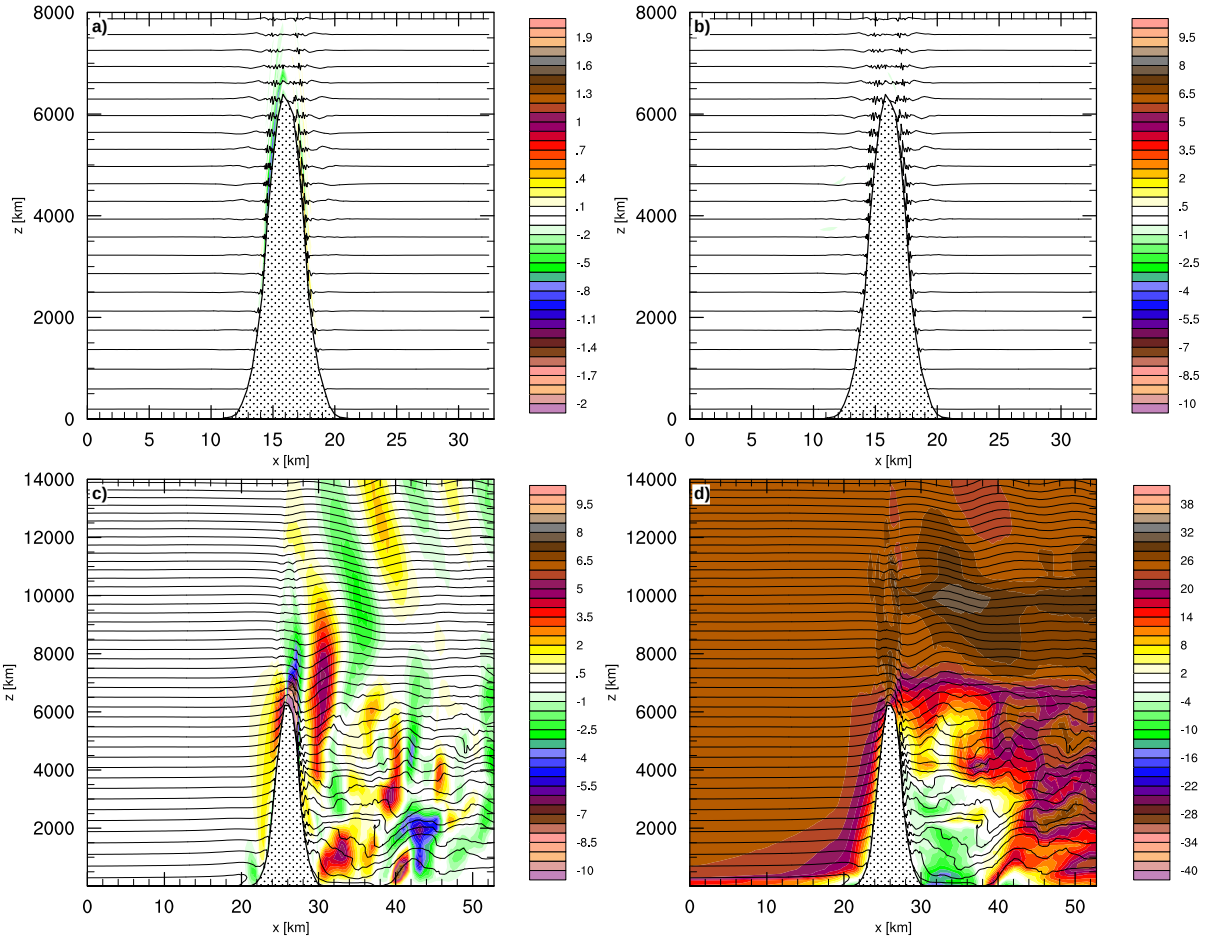

Figure 3: Results for experiments with a 7000-m high circular Gaussian mountain at t = 6 h with a maximum slope of about 3 with (a,b) an isothermal atmosphere at rest and (c,d) $U = 25\,\mathrm{m/s}$. Solid lines denote potential temperature (contour interval 4 K) and colour shading indicates (a,c) vertical or (b,d) horizontal wind speed (m/s) along the cross-section.

ICON experiment performs better than the GME reference run in all cases, indicating that the physics-dynamics coupling and the tuning of the physics parametrizations has reached a reasonably mature state. Even larger improvements are obtained in the tropics (not shown), primarily because ICON has smaller temperature biases than GME because of its more advanced convection and radiation parametrizations. Sensitivity tests with higher resolution (13 km, as envisaged for operational use) indicate that the gain of forecast quality with increasing resolution is larger in winter than in summer. Apart from that, the model behaviour depends fairly little on the horizontal resolution (at least for mesh sizes of 40 km or finer), which is important for the design of an ensemble data assimilation and forecasting system.

The skill scores can be put in relation to the computational efficiency of ICON, which is considerably better than that of the GME despite the fact that the GME is hydrostatic whereas ICON is nonhydrostatic. Part of the efficiency gain comes from the time-splitting between dynamics and physics applied in ICON, which allows using larger time steps for the physics parametrizations, another major part is due to the horizontally explicit time-stepping scheme of ICON that requires much fewer communication calls per time step than the iterative elliptic solver of GME. For the current operational GME setup—20 km mesh size with 60 levels—ICON needs about one quarter of the computational resources of GME to complete a seven-day forecast within one hour.

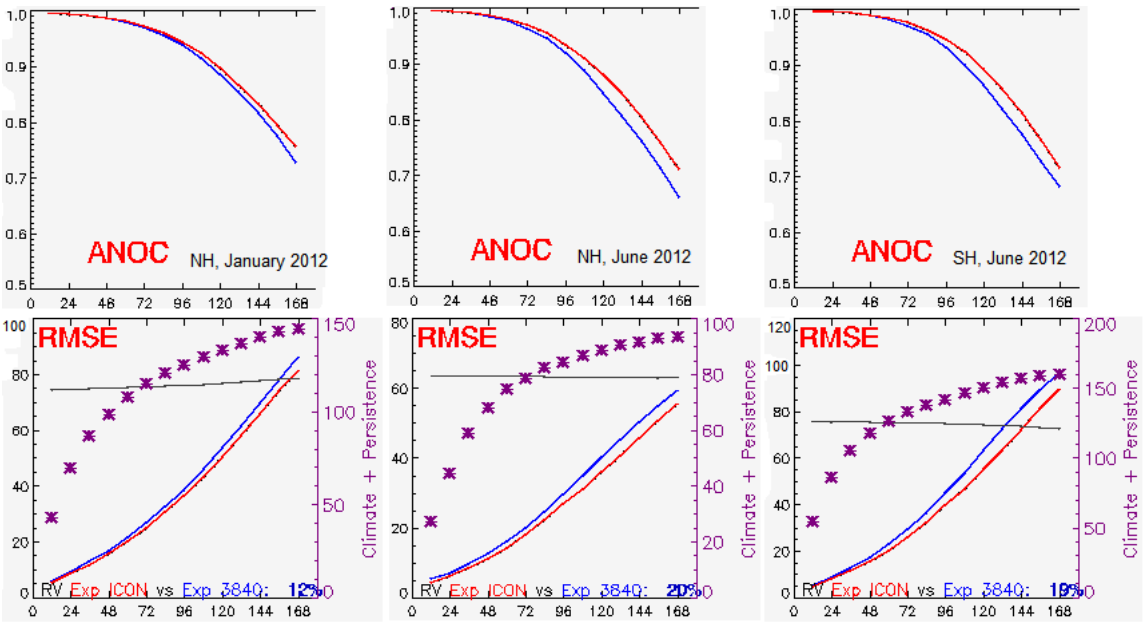

Figure 4: WMO standard skill scores for GME (blue lines) and ICON (red lines) with IFS initialization: 500 hPa geopotential anomaly correlation (upper row) and corresponding RMS error (gpm) for northern hemisphere, January 2012 (left), northern hemisphere, June 2012 (middle), and southern hemisphere, June 2012 (right). Blue numbers in the bottom row denote the reduction of the variance of GME vs. ICON; positive values indicate that ICON has smaller errors. Forecast hours are given on the abscissa.

4 Conclusions

Based on the current development state of the ICON model, it can be concluded that most of the major goals formulated in the initial planning phase have already been reached. The nonhydrostatic dynamical core provides exact mass conservation and tracer mass consistency, and has been successfully tested over a resolution range of three orders of magnitude, reaching from scales of several hundreds of kilometres down to scales of several hundreds of metres. A particular advantage over comparable dynamical cores using the fully compressible atmospheric equations is its higher numerical stability over steep slopes. A highly flexible implementation of static mesh refinement is available, allowing the use of multiple nested domains per nesting level and even to mix one-way nesting with two-way nesting within the same model run. Moreover, nested domains may be geometrically non-contiguous, and can have a lower top than their respective parent domain. The flow control implemented for the grid nesting includes an option for a limited-area mode, which in the longer-term future offers the possibility to fully replace the regional COSMO model in cooperation with our COSMO partners and thus to achieve a unified modelling system for all scales. Preliminary NWP tests with interpolated IFS analysis data indicate significantly better scores than for the GME, the current operational global forecasting model at DWD. On the other hand, the computational efficiency of ICON is superior to that of GME despite the fact that the latter is hydrostatic. This is partly related to a more efficient time integration scheme, allowing for larger time steps for tracer transport and the physics parametrizations, and partly to the lower amount of MPI communication needed in ICON.

Acknowledgements

The author wants to thank all members of the ICON development teams at the German Weather Service and the Max-Planck Institute for Meteorology for their excellent work, providing the basis for the summary report given in this article.

References

Bechtold, P., M. Köhler, T. Jung, F. Doblas-Reyes, M. Leutbecher, M. Rodwell, F. Vitart, and G. Balsamo (2008). Advances in simulating atmospheric variability with the ECMWF model: From synoptic to decadal time-scales. *Quart. J. Roy. Meteor. Soc 134*, 1337–1351.

Doms, G. and U. Schättler (2004). A description of the nonhydrostatic regional model LM. Part II: Physical parameterization. Technical report, Deutscher Wetterdienst, Offenbach, Germany. (available from http://www.cosmo-model.org/public/documentation.htm).

Gassmann, A. and H.-J. Herzog (2008). Towards a consistent numerical compressible non-hydrostatic model using generalized hamiltonian tools. *Quart. J. Roy. Meteorol. Soc. 65*, 1597–1613.

Heise, E., B. Ritter, and E. Schrodin (2006). Operational implementation of the multilayer soil model TERRA. Technical report, Deutscher Wetterdienst, Offenbach, Germany. (available from http://www.cosmo-model.org/public/documentation.htm).

Jablonowski, C. and D. Williamson (2006). A baroclinic instability test case for atmospheric model dynamical cores. *Quart. J. Roy. Meteorol. Soc. 132*, 2943–2975.

Klemp, J. B. and W. C. Skamarock (2003). Numerical consistency of metric terms in terrain-following coordinates. *Mon. Wea. Rev. 131*, 1229–1239.

Lauritzen, P. H., P. A. Ullrich, C. Jablonowski, P. A. Bosler, D. Calhoun, A. J. Conley, T. Enomoto, L. Dong, S. Dubey, O. Guba, A. B. Hansen, E. Kaas, J. Kent, J.-F. Lamarque, M. J. Prather, D. Reinert, V. V. Shashkin, W. C. Skamarock, B. Sørensen, M. A. Taylor, and M. A. Tolstykh (2013). A standard test case suite for two-dimensional linear transport on the sphere: results from a collection of state-of-the-art schemes. *Geoscientific Model Development Discussions 6*(3), 4983–5076.

Lott, F. and M. Miller (1997). A new subgrid-scale orographic drag parametrization: Its formulation and testing. *Quarterly Journal of the Royal Meteorological Society 123*(537), 101–127.

Majewski, D., D. Liermann, P. Prohl, B. Ritter, M. Buchhold, T. Hanisch, G. Paul, W. Wergen, and J. Baumgardner (2002). The operational icosahedral-hexagonal gridpoint model GME: Description and high-resolution tests. *Mon. Wea. Rev. 130*, 319–338.

Miura, H. (2007). An upwind-biased conservative advection scheme for spherical hexagonal-pentagonal grids. *Mon. Wea. Rev. 135*, 4038–4044.

Mlawer, E. J., S. J. Taubman, P. D. Brown, M. J. Iacono, and S. A. Clough (1997). Radiative transfer for inhomogeneous atmospheres: RRTM, a validated correlated-k model for the longwave. *J. Geophy. Res. 102*, 16663–16682.

Orr, A., P. Bechtold, J. Scinocca, M. Ern, and M. Janiskova (2010). Improved middle atmosphere climate and forecasts in the ecmwf model through a nonorographic gravity wave drag parameterization. *Journal of Climate 23*(22), 5905–5926.

Raschendorfer, M. (2001). The new turbulence parameterization of LM. *COSMO Newsletter 1*, 89–97. (available from http://www.cosmo-model.org).

Schär, C., D. Leuenberger, O. Fuhrer, D. Lüthi, and C. Girard (2002). A new terrain-following vertical coordinate formulation for atmospheric prediction models. *Mon. Wea. Rev 130*, 2459–2480.

Seifert, A. (2008). A revised cloud microphysical parameterization for COSMO-LME. *COSMO Newsletter 8*, 25–28. (available from http://www.cosmo-model.org).

Skamarock, W. C., J. B. Klemp, M. G. Duda, L. D. Fowler, S.-H. Park, and T. D. Ringler (2012). A multiscale nonhydrostatic atmospheric model using centroidal voronoi tesselations and C-grid staggering. *Mon. Wea. Rev. 140*, 3090–3105.

Wan, H., M. A. Giorgetta, G. Zängl, M. Restelli, D. Majewski, L. Bonaventura, K. Fröhlich, D. Reinert, P. Ripodas, L. Kornblueh, and J. Förstner (2013). The ICON-1.2 hydrostatic atmospheric dynamical core on triangular grids – Part 1: Formulation and performance of the baseline version. *Geosci. Model Dev. 6*, 735–763.

Zängl, G. (2012). Extending the numerical stability limit of terrain-following coordinate models over steep slopes. *Mon. Wea. Rev. 140*, 3722–3733.